

Multiscale Examination of Strain Effects in Nd-Fe-B Permanent Magnets

Min Yi,^{*} Hongbin Zhang,[†] Oliver Gutfleisch,[‡] and Bai-Xiang Xu[§]

Institute of Materials Science, Technische Universität Darmstadt, 64287 Darmstadt, Germany
(Received 12 January 2017; revised manuscript received 14 June 2017; published 12 July 2017)

We perform a combined first-principles and micromagnetic study on the strain effects in Nd-Fe-B permanent magnets. First-principles calculations on Nd₂Fe₁₄B reveal that magnetocrystalline anisotropy (K) is insensitive to deformation along the c axis, and that a - b in-plane shrinkage is responsible for K reduction. The predicted K is more sensitive to lattice deformation than the previous phenomenological model suggests. The biaxial and triaxial stress states have a greater impact on K . Negative K occurs in a much wider strain range in the a - b biaxial stress state. Micromagnetic simulations of Nd-Fe-B magnets using first-principles results show that a 3% to 4% local strain in a 2-nm-wide region near the interface around the grain boundaries and triple junctions leads to a negative local K and thus, remarkably, decreases the coercivity by about 60%, or 3 to 4 T. The local a - b biaxial stress state is more likely to induce a large loss of coercivity. In addition to the local stress states and the strain levels themselves, the shape of the interfaces and the intergranular phases also makes a difference. Smoothing the edge and reducing the sharp angle of the triple regions in Nd-Fe-B magnets would be favorable for a coercivity enhancement.

DOI: 10.1103/PhysRevApplied.8.014011

I. INTRODUCTION

Strain can be utilized to tailor the magnetic properties of many materials, leading to either promising applications or undesirable problems. For example, strain effects in soft magnetic materials can be used for the electric control of magnetic properties by using the strain-mediated magnetoelectric coupling [1,2]. In addition, strain-mediated magnetization switching has been a potential way of revolutionizing the spintronic devices that currently utilize power-dissipating currents [3–7]. In the permanent magnets which are featured in high-coercivity and high-maximal-energy products, local strain around the grain boundaries and triple junctions is thought to reduce the local magnetocrystalline anisotropy—and thus the coercivity [8–14]—degrading the magnetic performance. This fact indicates strain as a double-edged sword in magnetic materials. Understanding strain's effects is a prerequisite for a wise application or avoidance of this double-edged sword.

In this work, we focus on the strain effects in a typical permanent magnet, Nd-Fe-B. In Nd-Fe-B magnets, strain effects are inevitable. On the one hand, sintering processes, post-thermal treatments, and hot pressing unavoidably induce a certain residual strain. Such strain can be either at the bulk level or at the local level. On the other hand, the coercivity of standard Nd-Fe-B magnets is only about 20% of the theoretical upper limit from the Stoner-Wohlfarth model. The huge deviation from the theoretical prediction

is believed to be mainly originated from the microstructural effects [8,15–18]. The critical microstructural features that affect the coercivity are the intergrain phases and the grain-boundary phases. The structural or crystal-orientation mismatch between the Nd₂Fe₁₄B main phase and other phases will generate local strain near the interfaces of different phases or grains. It is possible that such local strain results in regions of reduced anisotropy as nucleation sites for reversal domains.

For the theoretical study of strain effects in Nd-Fe-B magnets, by using the phenomenological theory regarding magnetoelastic anisotropy [19], Hrkac and co-workers [9,11–14] and Kubo *et al.* [10] used molecular dynamics (MD) to determine the strain-induced anisotropy constant (K_{me}). However, depending on the interatomic potential used in MD, the value of the calculated K_{me} can differ by 1 order of magnitude. For example, based on a pairwise-interaction model for Nd₂Fe₁₄B, Hrkac and co-workers considered various crystal structures and crystal orientations of Nd and Nd oxides and evaluated maximum values of $K_{me} \sim -10$ to -4000 MJ/m³ in single atoms (the average K_{me} for all atoms is approximately -1 to -10 MJ/m³) in a local region of about 2 nm [9,11,12]. By contrast, Kubo *et al.* [10] developed an alternative angular-dependent potential model for Nd₂Fe₁₄B and estimated K_{me} as on the order of -0.1 MJ/m³ within a roughly 2-nm region. However, no experimental results have directly verified this 2-nm local region with extremely reduced magnetocrystalline anisotropy. In fact, early experiments showed that the homogeneous thermal strain present at the boundaries of Nd₂Fe₁₄B grains has only a small influence on the coercivity [19]. More recently, Murakami and co-workers [20,21] directly measured the

^{*}yi@mfm.tu-darmstadt.de

[†]hzhang@tmm.tu-darmstadt.de

[‡]gutfleisch@fm.tu-darmstadt.de

[§]xu@mfm.tu-darmstadt.de

strain distribution around different interfaces in sintered Nd-Fe-B magnets. They demonstrated that the region with a strain of $\epsilon_c \sim \pm 1\%$ extends over several tens of nanometers (not the theoretical prediction of approximately 2 nm confined to a local region) away from the interface. Similar to the early experiments [19], they also speculated that the interfacial strains have limited influence on the coercivity. One plausible reason for the inconsistency between simulations and experiments is the experimental resolution limitations; i.e., presently, it is difficult to measure the strain within about a 2-nm-wide local region in these experiments [20]. Therefore, in terms of the inconsistency not only between previous MD simulations themselves but also between the simulations and experimental measurements up to now, in the modeling aspect, it is required that this issue be more precisely investigated at a quantitative or multiscale level.

In this work, we perform a combined first-principles and micromagnetic study on Nd-Fe-B magnets to demonstrate a multiscale simulation framework for elucidating the strain effects on Nd-Fe-B magnets and to clarify what kind(s) of local strain can significantly reduce the coercivity. Previous first-principles calculations have provided insights into the magnetic moments and the magnetocrystalline anisotropy based on either the crystal field of Nd ions [22–27] or the total energy difference [28,29]. Specifically, Suzuki *et al.* [23] explored the crystal-field parameter of Nd ions in the case of changing the length of the a and c axes. Asali *et al.* [30] showed the dependence of magnetic anisotropy on a c/a ratio of $X_2Fe_{14}B$ ($X = Y, Pr, Dy$), and Torbatian *et al.* [31] examined triaxial strain effects on the magnetic anisotropy in $Y_2Fe_{14}B$. However, they did not report results for $Nd_2Fe_{14}B$. Therefore, strain effects of $Nd_2Fe_{14}B$ in different forms and magnitudes scrutinized from first principles are still of interest. By using the first-principles results as inputs, we carry out further micromagnetic simulations to elucidate the strain effects on the coercivity of single- and multigrain Nd-Fe-B magnets.

II. METHODOLOGY

The first-principles calculations are carried in the framework of the projector-augmented-wave formalism as implemented in the Vienna *ab initio* simulation package [32]. The Perdew-Burke-Ernzerhof exchange-correlation functional in the generalized-gradient approximation is employed [33]. According to previous work [28], an energy cutoff of 400 eV and a Monkhorst-Pack k mesh $5 \times 5 \times 4$ are utilized to reach a good convergence. The convergence criteria for the full structure relaxation at different stress states and strain levels are set at 10^{-5} eV and 10^{-3} eV/Å for the energies and forces, respectively [28]. To obtain the magnetocrystalline anisotropy (K), $4f$ electrons are treated as valence electrons [28]. Non-self-consistent calculations with different spin quantization axes are made by including spin-orbit coupling, starting from self-consistent charge

densities of spin-polarized calculations. In this way, K is evaluated as the change of such total energies when the magnetization is along different axes, i.e.,

$$K = \begin{cases} [\max(E_a, E_b) - E_c]/V & (E_a > E_c \text{ and } E_b > E_c) \\ [\min(E_a, E_b) - E_c]/V & (E_a < E_c \text{ or } E_b < E_c) \end{cases}, \quad (1)$$

in which V is the volume of the relaxed unit cell. E_a , E_b , and E_c are the total energies when the magnetization is parallel to the a , b , and c axes, respectively. A positive K indicates easy axis along the c axis, while a negative K indicates an easy a - b plane.

Using K and M_s (saturation magnetization) obtained from first-principles calculations as functions of stress states and strain levels, micromagnetic simulations are carried out with the 3D National Institute of Standards and Technology OOMMF code [34] for solving the Landau-Lifshitz-Gilbert equation [35–37]. Single- and multigrain Nd-Fe-B magnets are discretized by cubic meshes with a size of 1 nm. For the single grain, prisms with different sectional geometry are considered. For modeling the multigrain, we use the scanning-electron-microscopy (SEM) image of a sintered Nd-Fe-B magnet from previous experiments [20]. The exchange constant is set at 12.5 pJ/m [38]. Hysteresis curves are calculated by setting the initial magnetization along a positive c axis and the external field along a negative c axis.

III. RESULTS AND DISCUSSION

A. First-principles calculations of strained $Nd_2Fe_{14}B$

Figures 1 and 2 present the first-principles results of K and M_s under various stress states and strain levels up to $\pm 7\%$. Bulk-level homogeneous strain in the abovementioned range in a real $Nd_2Fe_{14}B$ magnet is not realistic. However, there are several plausible sources of the very large local strain, such as lattice or crystal orientation mismatch between $Nd_2Fe_{14}B$ grains and the intergranular phases, thermal residual stress at triple regions, grain irregularity for stress concentration, symmetry breaking at the grain surface or near the interface, etc. In addition to these possible experimental phenomena, other reasons for introducing large strain range in this theoretical work fall under three aspects. First, Hrkac and co-workers [9,11,12,14] and Kubo *et al.* [10] adopted MD simulations and, indeed, predicted a significant change in K that is caused by the very large local strain within about a 2-nm narrow interface region. Second, to date, no experimental data on the strain in this localized region are available. The question regarding the magnitude of the extremely localized strain near the interface is still open from the experimental viewpoint. Third, large strain is possible in the local region. It is well known in mechanics that the theoretical strength of a material (inversely proportional to

the square root of the atomic-layer distance) can be 3 orders higher than the measurable fracture toughness (inversely proportional to the square root of the microcrack length) [39]. Therefore, the grain surface layer of 2 nm can sustain large deformations without fracture. Also, as shown in previous MD simulations [9–12,14], local atomic arrangements at the grain boundaries or interfaces experience dramatic change, but they are still stable without fracture. The locally dramatic change in atomic arrangements can be considered a large effective strain which is confined to the vicinity of the interfacial region. Our theoretical calculations are suggested as a first step to cover such a case in order to see what would occur there. Based on the above considerations, we introduce a large strain range (but still smaller than the strain values predicted by previous MD simulations) in this work. By inputting the strain-dependent first-principles results to the micromagnetic model with a locally strained region of approximately 2 nm, we attempt to reveal the local-strain effects on the coercivity. This theoretical work could be considered a plausible first step towards a more accurate study by combining experimental local-strain measurement and theoretical calculations of an interface-containing large supercell with several hundred atoms. In the stress-free $\text{Nd}_2\text{Fe}_{14}\text{B}$ unit cell, our first-principles calculations show a K value of approximately 5.1 MJ/m^3 (about $30.1 \text{ meV/unit cell}$) and an M_s value of approximately 1.525 MA/m . The calculated K agrees well with the experimental results [40–44], as indicated by the five horizontal lines in Fig. 1(a). The calculated M_s is about $38.3 \mu_B/\text{formula units (f.u.)}$, which also matches well with the experimental value of approximately $37.7 \mu_B/\text{f.u.}$ [45] and other first-principles results [46–48]. The consistence between our calculations and the experimental results validates our first-principles study on $\text{Nd}_2\text{Fe}_{14}\text{B}$.

The calculated M_s in Figs. 1 and 2 shows that it is not remarkably influenced by the stress states and strain levels, except for the severer triaxial stress state in the lower left-hand corner of Fig. 2(f). However, the calculated K is highly dependent on both the stress states and the strain levels. In the c uniaxial stress state in which only the crystal axis c of $\text{Nd}_2\text{Fe}_{14}\text{B}$ is stressed and other two crystal axes a and b are stress-free or free to relax, K shows a decreasing trend as the strain ε_c is increased, as shown in Fig. 1(a). On the contrary, Fig. 1(c) indicates that K increases with the strain ε_a when an a uniaxial stress is applied. Figure 1(e) shows that the pure shear in the a - b plane has a negligible effect on K when the shear strain γ_{a-b} is less than 10%. Only in the extremely sheared case ($\gamma_{a-b} > 15\%$) is K remarkably reduced. Since the hydrostatic pressure up to approximately 5.3 GPa induces a tiny shrinkage of the lattice, it only slightly reduces K , as shown in Fig. 1(g), which is a special case of Fig. 2(e). For the hydrostatic pressure in Fig. 1(g), the stress in all three directions is the same. While, for the triaxial stress state in Fig. 2(e), the stress along the a (b) axis and the stress along the c axis can

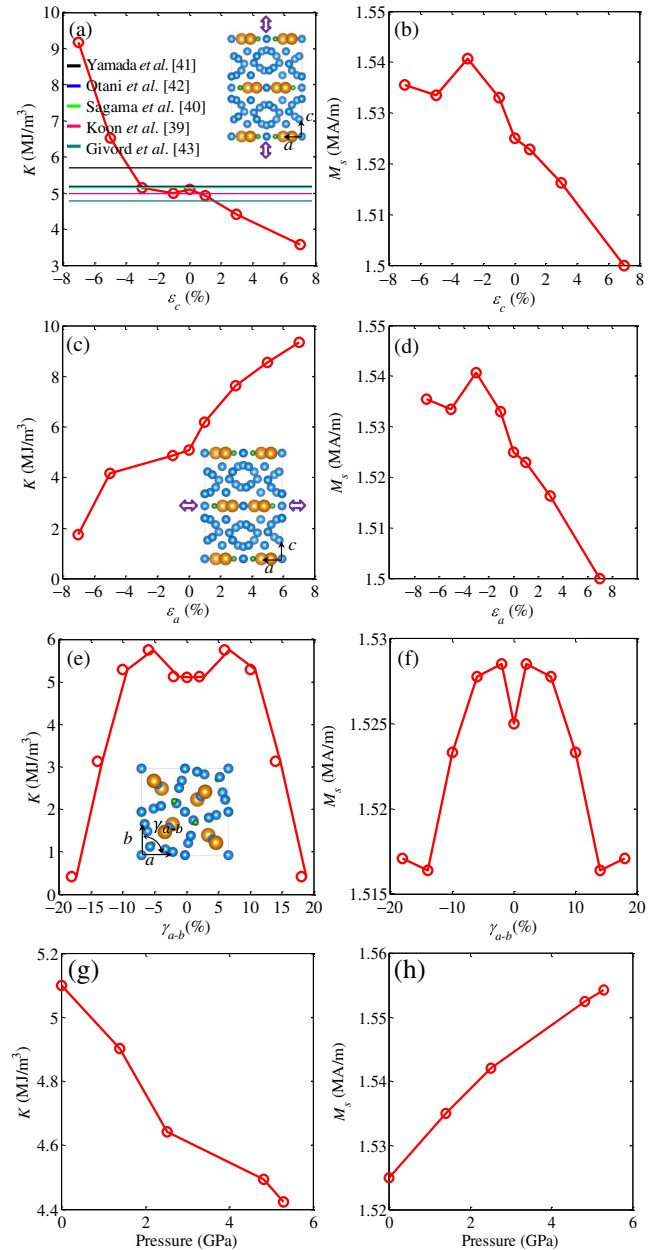


FIG. 1. First-principles-calculated K and M_s in the stress state of (a), (b) c uniaxial stress, (c), (d) a uniaxial stress, (e), (f) pure shear in the a - b plane, and (g), (h) hydrostatic pressure. The inset lines in (a) correspond to the experimental results of an unstrained single crystal in the literature [40–44].

be either equal or not. The maximum hydrostatic pressure of about 5.3 GPa in Fig. 1(g) corresponds to a strain state of $\varepsilon_a = \varepsilon_b \sim 1.27\%$ and $\varepsilon_c \sim 1.47\%$. The results in Fig. 1(g) are consistent with those in the triaxial stress state shown in Fig. 2(e). The variation of K under biaxial and triaxial stress states is presented in Fig. 2. It is obvious that a negative K occurs in a much wider strain range in the a - b in-plane biaxial stress state, as shown in Fig. 2(a). The shrinkage in the a - b plane can notably reduce K . For example, a - b biaxial stress states with $\varepsilon_a = \varepsilon_b = -3\%$ and -4% reduce

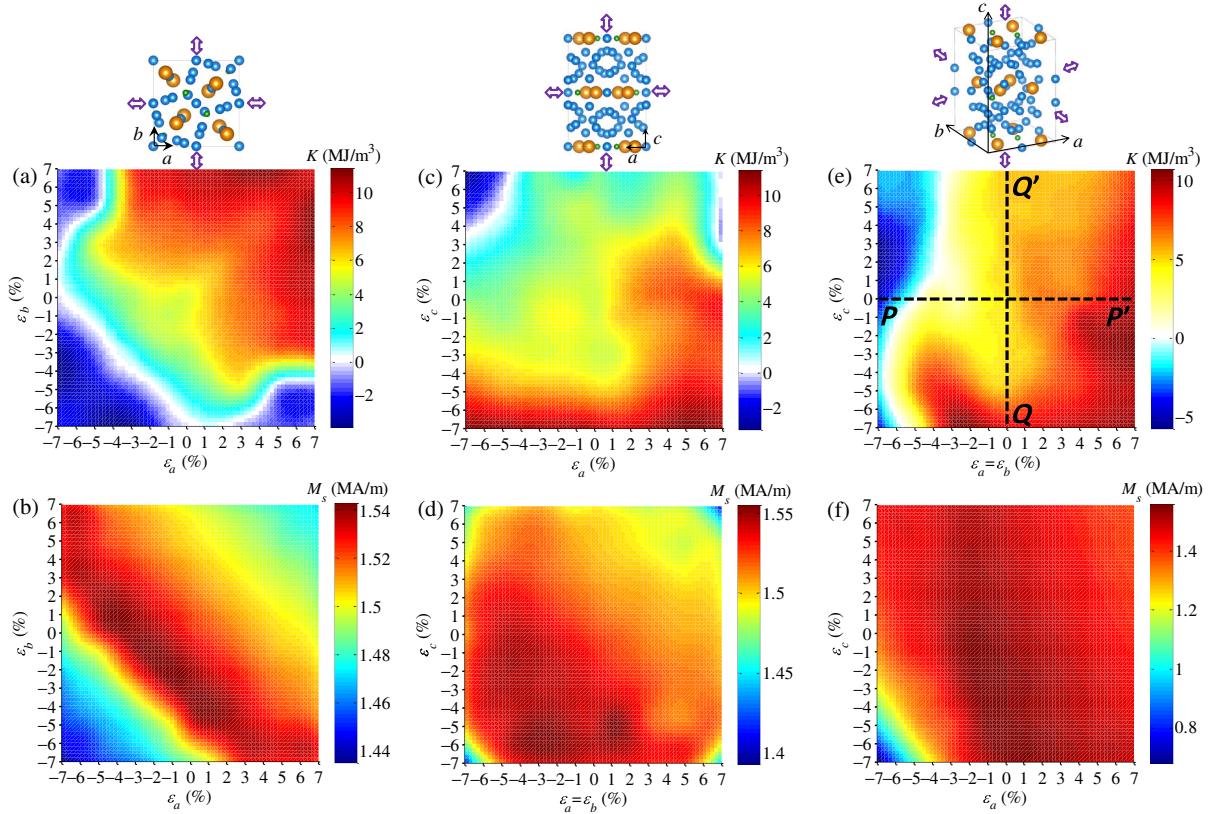


FIG. 2. First-principles-calculated K and M_s values in the stress states of (a), (b) a - b biaxial stress, (c), (d) a - c biaxial stress, and (e), (f) a - b - c triaxial stress.

K to approximately 1.4 and about -0.38 MJ/m³, respectively. By contrast, for the a - c biaxial stress in Fig. 2(c), the strain range for a negative K is very small. Only in the case of a negative ε_a or a large positive ε_c , K is reduced. For the a - b - c triaxial stress state in Fig. 2(e), a negative K appears for a large negative $\varepsilon_a = \varepsilon_b$. The c elongation and a - b plane shrinkage reduce K . For example, K decreases to about 2.1 MJ/m³ in the case of $\varepsilon_a = \varepsilon_b = -3\%$ and $\varepsilon_c = 3\%$. The results in Fig. 2(e) agree well with the previous work by calculating the crystal-field parameters of Nd ions [23] and are qualitatively consistent with the results from MD simulations [9–12].

From the results in Figs. 1(a) and 1(c), one might think that the shrinkage along a and c has opposite effects on K . In fact, this is not the case. Owing to the positive Poisson effect, uniaxial tensile stress along the a (c) axis induces shrinkage along the c (a) axis. So under the uniaxial stress state [Figs. 1(a) and 1(c)], the interference between the strain along the a and c axes makes it difficult to judge the main influential factor for K . Then we consider the triaxial stress state in which we can either set strain along the c axis by forcing zero strains along a and b or set strain in the a - b plane by forcing zero strains along the c axis, as indicated by the two dashed lines in Fig. 2(e). For the line QQ' , i.e., the case of $\varepsilon_a = \varepsilon_b = 0$, K does not change so much when ε_c is larger than -6% . For the line PP' , i.e., the case of

$\varepsilon_c = 0$, K gradually changes from approximately 9.7 MJ/m³ to about -4.5 MJ/m³ when $\varepsilon_a = \varepsilon_b$ decreases from 7% to -7% . These results from lines PP' and QQ' indicate that K is insensitive to the deformation along c but changes, apparently, with the a - b in-plane deformation. In other words, the shrinkage in the a - b plane should be responsible for the K reduction. The decrease of K with an increasing ε_c in Fig. 1(a) is ascribed to the c elongation-induced a - b -plane shrinkage through the positive Poisson effect. This result also explains the results in Fig. 2 that a negative K always appears in the region with a negative ε_a or ε_b and a positive ε_c and a - b biaxial stress state allows a much larger strain range for a negative K .

In order to qualitatively understand the sign change of K , we analyze the valence charge density. The density map in the (001) plane of Nd₂Fe₁₄B is shown for three typical cases in Fig. 3. In order to clearly display the charge-density difference, the legend is scaled down to the range 0.02–0.03 e/bohr^3 . In this way, the charge-density difference around Nd atomic sites can be easily identified by the color, as indicated by the dashed circles in Figs. 3(a)–3(c). It can be found that the charge density at the Fe(c) sites exhibits a distorted distribution towards the B sites and forms an aspherical shape. The charge density at Nd(f) sites and Nd(g) sites is slightly different, but both deviate from the spherical distribution. The charge density at the B

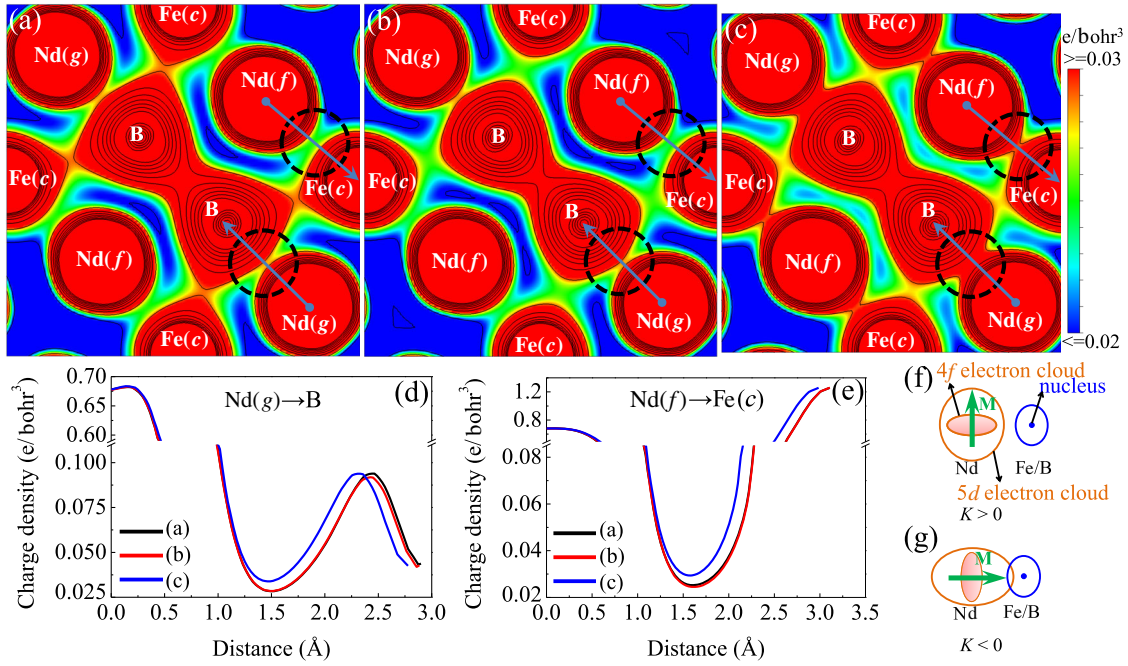


FIG. 3. Valence-electron-density distributions of $\text{Nd}_2\text{Fe}_{14}\text{B}$ in the (001) plane. (a) $\epsilon_a = \epsilon_b = \epsilon_c = 0$. (b) $\epsilon_a = \epsilon_b = 0$ and $\epsilon_c = 4\%$. (c) $\epsilon_a = \epsilon_b = -4\%$ and $\epsilon_c = 4\%$. The dashed circles indicate regions where the charge-density distribution around Nd atoms apparently changes. The charge-density distribution along the lines (d) $\text{Nd}(g) \rightarrow \text{B}$ and (e) $\text{Nd}(f) \rightarrow \text{Fe}(c)$ is indicated by arrows in (a)–(c). (f), (g) Schematics for a possible explanation of the sign of K [25].

sites is extremely anisotropic and is extended towards the $\text{Nd}(g)$ and $\text{Fe}(c)$ sites [49,50]. Despite these common features of the charge density, strain can induce some nontrivial changes. A comparison between Fig. 3(a) with no strain and Fig. 3(b) with $\epsilon_a = \epsilon_b = 0$ and $\epsilon_c = 4\%$ reveals only a slight change of the charge distribution around the $\text{Fe}(c)$ and B sites. Since no remarkable change of the charge distribution around the Nd sites is observed in Fig. 3(b), the sign of K remains the same as that in Fig. 3(a). This finding indicates that deformation along the c axis without in-plane strain (i.e., $\epsilon_a = \epsilon_b = 0$) does not remarkably change K , agreeing well with the above results. By contrast, if an additional in-plane shrinkage strain ($\epsilon_a = \epsilon_b = -4\%$) is applied, the charge distribution around Nd sites is notably altered, as shown by the dashed circles in Fig. 3(c). Moreover, the charge-density distribution along the lines $\text{Nd}(g) \rightarrow \text{B}$ [Fig. 3(d)] and $\text{Nd}(f) \rightarrow \text{Fe}(c)$ [Fig. 3(e)] also indicates an apparent increase of charge density around Nd when in-plane compressive strain is applied. Because of the reduction of the distance between the Nd and Fe/B sites, there is evidence of some degree of hybridization between the Fe/B atoms and the Nd atoms [Fig. 3(c)]. Through the hybridization, the 5d electron cloud of Nd atoms apparently extends towards the Fe/B atoms. The extension of 5d cloud relocates the 4f electron cloud perpendicular to the a - b plane in order to avoid the repulsive force from the horizontally extended 5d electron cloud [25], thus leading to an easy a - b plane and a negative K [Fig. 3(g)]. Therefore, one possible explanation is that

the in-plane shrinkage makes the Fe/B atoms much closer to the Nd atoms and results in a hybridization between them, which further changes the 5d electron cloud surrounding the 4f electron cloud of Nd atoms and finally alters the sign of K [25].

It should be noted that several researchers [9–12] have dealt with the strain-induced K change by using the phenomenological magnetoelastic coupling energy which was derived by de Groot and de Kort [19]. They calculated the strain-induced anisotropy constant (K_{me}) as a function of lattice strain and applied K_{me} to estimating the change of K by using the elastic constants from isotropic polycrystals. For a qualitative and order-of-magnitude analysis, we rewrite the K_{me} from de Groot and de Kort as $K_{\text{me}} \sim B\epsilon$, in which B denotes the magnetoelastic coefficient and ϵ the strain level. By using the parameters given in the literature [19], our estimation of B is shown to be on the order of 40 MJ/m^3 . This means that a large strain on the order of 10% can give a K change of only about 4 MJ/m^3 . For a negative K , a strain of more than 12% is required. However, our first-principles calculations show that a small strain of around 4% can even reduce K to negative values [Fig. 2(a)]. Hence, our first-principles study indicates a much larger sensitivity of K to the lattice deformation. The underestimation of strain effects by the phenomenological description could be attributed to the assumption of a one-ion magnetoelastic Hamiltonian without a two-ion one because the two-ion magnetoelasticity is also related to the modification of the two-ion magnetic interactions by the

strains [51]. In our first-principles calculations, however, both one- and two-ion magnetic interactions and full electron-lattice coupling are consistently included.

B. Micromagnetic simulations of locally strained Nd-Fe-B magnets

Previous experiments have demonstrated that homogeneous small strain in Nd-Fe-B magnets has negligible effect on the coercivity [19]. However, previous MD simulations verified that a large strain is possible in a very localized region about 2 nm wide near the interface [9–12]. The authors used the atomic displacement near the interface to calculate the local strain, which is then considered to be the lattice strain as inputs for the phenomenological magnetoelastic theory [19] to estimate the K change. In the micromagnetic simulations here, we also follow a similar idea discussed in previous studies [9–12,14,52]; i.e., the source of the local strain is not the focus and an effective lattice strain is assigned to the local region. The symmetry breaking and the change of chemical environments near the local region are beyond the scope in this work, although they can also influence the coercivity. However, unlike these previous studies, which used phenomenological theory [19], here, we directly take the lattice strains and stress states associated with the first-principles calculations to define the locally strained region in Nd-Fe-B magnets. The local region is set at approximately 2 nm thick, as demonstrated by the MD simulations [9–12,14]. The parameters K and M_s of the locally strained region under various strain levels and stress states are taken from the first-principles results presented above.

1. Single-grain Nd-Fe-B magnets

We first investigate the prism-shaped single grain, which is covered by a locally strained surface with a thickness of t . Figure 4(a) displays the grain shape of a hexagonal prism, with the geometry dimension of $h = 200$ nm, $d = 300$ nm, and $t = 2$ nm. If we assume that the grain surface is under the local a - b biaxial stress state, it can be found that, for the hexagonal prism, the coercivity decreases from 5.7 to 1.96 T under an a - b biaxial strain of $\varepsilon_a = \varepsilon_b = -5\%$ [Fig. 4(b)]. However, the coercivity increases by only 0.5 T in the case of $\varepsilon_a = \varepsilon_b = 5\%$. This indicates that the coercivity is more sensitive to the local region with a - b -plane shrinkage and a negative K .

We further study the effects of the grain shape of the locally strained single grain. The motivation is to explore the possible role of the place where strain or stress appears and the associated micromagnetic mechanism. The grain-shape effects have recently been investigated for achieving high coercivity [53–56]. Here, we consider four types of prism grains: those with triangular, rectangular, hexagonal, and circular sections. The distribution of the c component of the unit magnetization vector (m_c) at the remanent state ($\mu_0 H_{\text{ex}} = 0$) is presented in Fig. 4(c). It can be seen that the

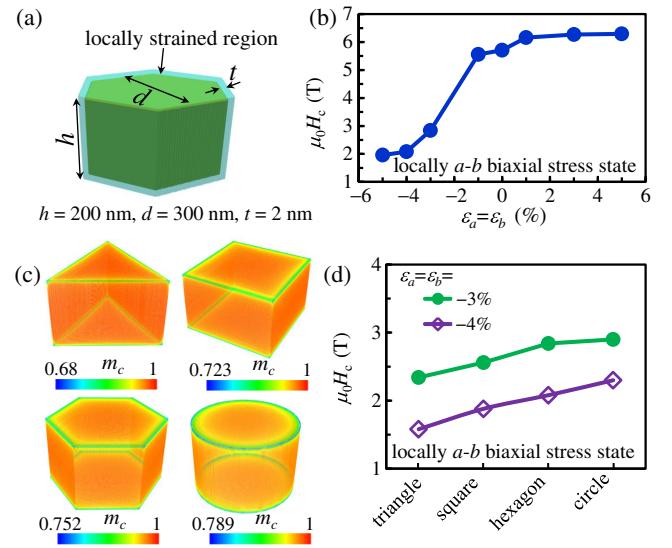


FIG. 4. (a) Schematic of a single-grain Nd-Fe-B magnet with a hexagonal section and with its surface covered by a locally strained region. (b) Local-strain-dependent coercivity for the grain in (a) under the local a - b biaxial stress state. (c) m_c distribution at the remanent state ($\mu_0 H_{\text{ex}} = 0$) for grains with triangular, square, hexagonal, and circular sections under a local a - b biaxial strain of -4% . (d) Coercivity for the grains in (c) under local a - b biaxial strains of -3% and -4% .

magnetization near the corners or edges has already rotated out of the easy direction even at the remanent state. More precisely, the minimum m_c values in Fig. 4(c) are found to decrease in the following order: circular prism $>$ hexagonal prism $>$ square prism $>$ triangular prism. This means that the local reversal occurs fastest in the triangular prism and slowest in the circular prism. Such a local reversal is due to the inhomogeneous stray field near the corners or edges in the nonellipsoidal grains [53,57]. By the local reversal, the inhomogeneous magnetization can suppress magnetic surface charges and decrease the stray-field energy with respect to the homogeneous magnetic state. The different local reversal behavior could result in distinct coercivity. We find in Fig. 4(d) that, at the same local stress states and strain levels, the coercivity is shown to increase in this order: triangular prism $<$ square prism $<$ hexagonal prism $<$ circular prism. For example, in the case of a local a - b biaxial stress state with $\varepsilon_a = \varepsilon_b = -4\%$, the coercivity is found to significantly increase from 1.58 T in the triangular prism to 2.3 T in the circular prism. These results indicate that, in addition to the local stress states and the strain levels themselves, where the locally strained region appears (e.g., grain shape, surface irregularity, and edge curvature) also plays an important role in determining the coercivity.

By using the hexagonal prism in Fig. 4(a), we carry out a detailed study on the sensitivity of the coercivity to the local stress states and strain levels. The coercivity change distribution in Fig. 5 is similar to the K distribution in

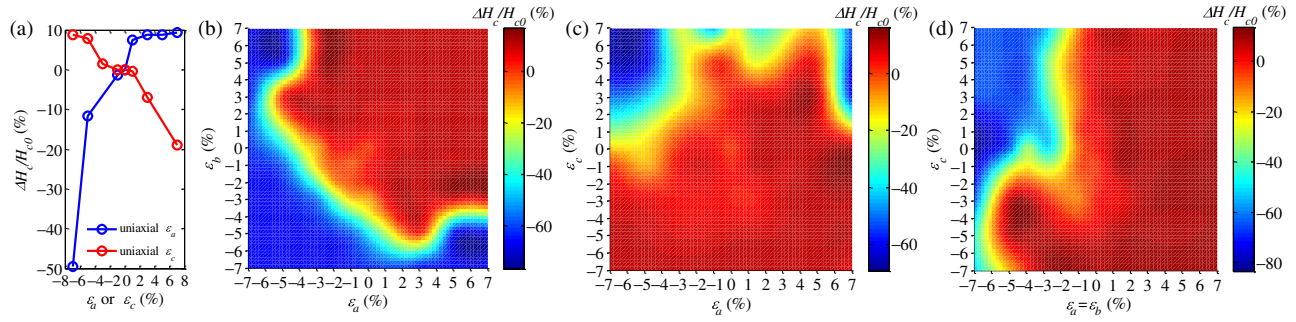


FIG. 5. Micromagnetic simulation results on the coercivity change as functions of the local surface strain under the stress state of (a) uniaxial stress, (b) a - b biaxial stress, (c) a - c biaxial stress, and (d) a - b - c triaxial stress. The micromagnetic mode is single Nd-Fe-B grain with a hexagonal section in Fig. 4(a).

Figs. 1 and 2. We find that, in all of the cases, the coercivity enhancement is limited to about 10%, while the coercivity decrease can be about as high as 80%. Again, the coercivity decrease is found to be more sensitive to the local strain than the coercivity enhancement. Figure 5(a) shows that the uniaxial stress states along the c and a axes induce maximum coercivity decreases of approximately 20% and about 50%, respectively. The local a - b biaxial stress state allows a much larger strain range for a coercivity decrease of about 60%, as shown in Fig. 5(b). By contrast, the local a - c biaxial and a - b - c triaxial stress states have a much smaller strain range for the coercivity decrease, as shown in Figs. 5(c) and 5(d).

2. Multigrain Nd-Fe-B magnets

Micromagnetic simulations on the multigrain are further performed. The multigrain model in Fig. 6(a) is built by

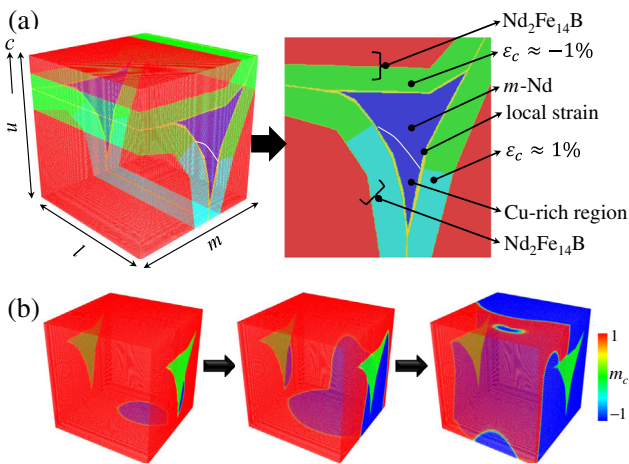


FIG. 6. Micromagnetic simulation of a multigrain based on the SEM image of the experimental work [20]. (a) Model illustration with the size of $l = m = 280$ nm and $n = 300$ nm. The locally strained region has a width of approximately 2 nm. (b) The magnetic reversal process between the external fields of -1.96 and -1.98 T when the local region is under a biaxial stress state with $\epsilon_a = \epsilon_b = -4\%$.

using the SEM image of a sintered Nd-Fe-B magnet [20]. The size $m = 280$ nm and $n = 300$ nm is estimated from the SEM image. Around the triple junction, the region with a strain of $\epsilon_c = \pm 1\%$ is extended over several tens of nanometers away from the interface, as measured in previous experimental work [20]. An additional locally strained region with a 2-nm width is assumed in the interface, as was done in previous work [9,11,12]. Owing to the small size of the model, the simulated coercivity without local strain is about as high as 5.84 T, as shown in Fig. 7. The effect of the strain $\epsilon_c = \pm 1\%$ extending over several tens of nanometers on the coercivity is negligible, further confirming a statement in a previous experimental work [20]. It can be seen from Fig. 7 that, in the case of local uniaxial stress states, the strain has little

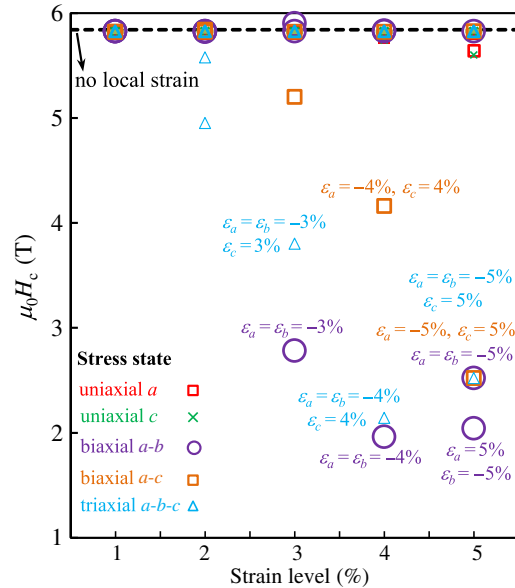


FIG. 7. Coercivity of the multigrain as functions of the local stress states and strain levels. The dashed line indicates the coercivity in the case with no local strain. Each color denotes one stress state of the local region. The strain values are marked when the coercivity decrease is over 1 T.

influence on the coercivity. However, the biaxial and triaxial stress states remarkably reduce the coercivity. An a - b biaxial stress state with $\varepsilon_a = \varepsilon_b = -4\%$ and -3% decreases the coercivity from 5.84 to 1.98 and 2.8 T or by about 66% and 52%, respectively. This means that a moderate strain level in a suitable local stress state can reduce the coercivity in the multigrain Nd-Fe-B magnets by more than 3 T. The magnetic reversal process in Fig. 6(b) indicates several apparent nucleation sites in the locally strained region. Then the reversal domain rapidly expands and the whole grain completely reverses instantly.

By using the first-principles results in Figs. 1 and 2, we calculate the coercivity of the multigrain as functions of the local stress states and strain levels, as shown in Fig. 7. It is found that the local uniaxial stress states almost do not affect the coercivity. Only the strain values marked in Fig. 7 and their associated stress states can reduce the coercivity by more than 1 T. Obviously, the local a - b biaxial stress state possesses a higher possibility to result in more reduction in the coercivity. In the case of local a - b biaxial and a - b - c triaxial stress in Fig. 7, though 5% strain induces a larger negative value of K than 4% strain, the coercivity is slightly increased. This is due to the fact that a local negative K favors the formation of an initial 90° domain wall between the locally strained region and the strain-free region, but a more negative K increases the field for the subsequent formation of a 180° domain wall. This result also indicates that a larger negative value of local K inducing more reduction in the coercivity is not always correct.

Owing to the small mesh size (1 nm here) determined by the physical length in micromagnetic simulations, the sample size of the modeled multigrain is often much smaller than that of the real magnets. In order to present an example for demonstrating the size effect, we increase the multigrain size here by extending l [Fig. 6(a)] to $1.4 \mu\text{m}$, as shown in the

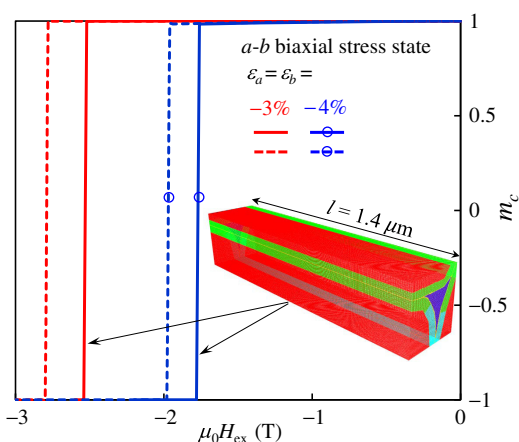


FIG. 8. Simulated reversal curves of the multigrain with the local-strain region under the a - b biaxial stress state ($\varepsilon_a = \varepsilon_b = -3\%$ and -4%). The solid lines correspond to the model in the inset with $l = 1.4 \mu\text{m}$. The dashed lines correspond to the model in Fig. 6(a).

inset of Fig. 8. Such an extension results in a mesh number of approximately 0.12×10^9 , which is extremely computationally expensive. From the reversal curves in Fig. 8, it can be seen that in local a - b biaxial stress states with either $\varepsilon_a = \varepsilon_b = -4\%$ or $\varepsilon_a = \varepsilon_b = -3\%$, the increase of l from 280 nm to $1.4 \mu\text{m}$ makes the coercivity decrease by about 0.3 T. The coercivity reduction can be qualitatively understood from the demagnetization effect. The l extension favors a reduction and an increase of the demagnetization factor along the l and c directions, respectively. The effect of l extension increases the in-plane shape anisotropy and exerts additional torque to make magnetization deviate from the c axis, thus resulting in premature nucleation and reduced coercivity.

Finally, it is worth mentioning that the single-grain results in Fig. 5(d) inspire a strategy of increasing the coercivity by tuning the shape or geometry of the local-strain region in the multigrains. By this inspiration, we then change the model in Fig. 6(a) into an ideal model whose triple region is set as a circular prism, as shown in the inset of Fig. 9, in order to study the effect of where the local strain appears. In contrast to Fig. 6(a), in which the local strain is in the triangular edge of the triple region, the model in Fig. 9 puts the local strain in the circular edge. We can find from Fig. 9 that the coercivity is obviously enhanced if a circular prism is used to represent the triple region. This is consistent with the result from the single-grain study and indicates the shape of the triple region as an influential factor for the coercivity. Smoothing the edge and removing the sharp angle of the triple region are favorable for coercivity enhancement. It should be noted that the circularly shaped triple region presented in the simulation is an ideal case, but it provides practical information towards coercivity enhancement. In realistic conditions, though achieving a perfectly circular triple region is

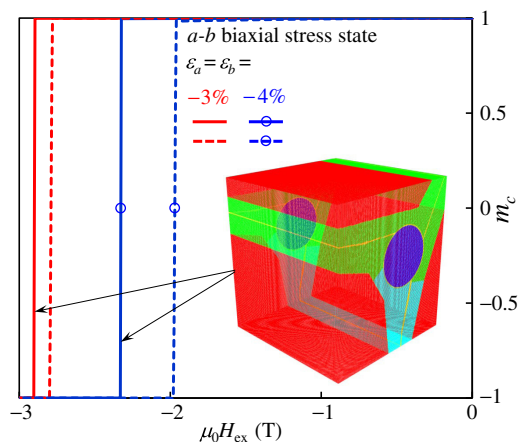


FIG. 9. Simulated reversal curves of the multigrain with the local-strain region under the a - b biaxial stress state ($\varepsilon_a = \varepsilon_b = -3\%$ and -4%). Solid lines correspond to the model in the inset with a circularly shaped triple region. The dashed lines correspond to the model in Fig. 6(a).

difficult, reducing the sharp angle of the triple regions or making them as smooth as possible in Nd-Fe-B magnets is possible by using gas-atomized powders, controlled grain-boundary diffusion, or additive manufacturing.

IV. CONCLUSIONS

Strain effects in Nd-Fe-B magnets are examined by a combined first-principles and micromagnetic study. In this way, we use the first-principles results on the stress states and strain levels dependent on K and M_s as the input for micromagnetic simulations of the coercivity in single- and multigrain Nd-Fe-B magnets. The main conclusions are summarized in the following:

- (1) In the Nd₂Fe₁₄B phase, the stress states and strain levels have negligible effects on M_s but significant effects on K . K is sensitive to the a - b in-plane deformation rather than the c -axis deformation. The a - b -plane shrinkage is responsible for the K reduction. The biaxial and triaxial stress states have a greater impact on K than other stress states. A negative K occurs in a much wider strain range in the a - b biaxial stress state.
- (2) K is shown to be more sensitive to the lattice deformation by the first-principles study than by the previous phenomenological model [19], which considers only one-ion magnetoelastic Hamiltonian and underestimates the strain effects. An a - b biaxial stress state with $\epsilon_a = \epsilon_b = -3\%$ and -4% reduces K to about 1.4 and approximately -0.38 MJ/m³, respectively.
- (3) In Nd-Fe-B magnets, the local a - b biaxial stress state in the locally strained region is more likely to induce a large loss of coercivity. A coercivity decrease by 60% or by 3 to 4 T can be induced by a 3% to 4% local strain in a 2-nm-wide region near the interface around the grain boundaries and triple junctions.
- (4) In addition to the local stress states and the strain levels themselves, the shape of the interfaces and the intergranular phases also makes a difference. Smoothing the edge and reducing the sharp angle of the triple regions in Nd-Fe-B magnets would be favorable for a coercivity enhancement.

It is anticipated that our multiscale results here based on first-principles calculations and micromagnetic simulations will provide quantitative information regarding that what kind of local stress state and how large a local strain can induce a significant decrease in coercivity. The results will also be applied to the high-resolution experimental research of the local-strain measurement in Nd-Fe-B permanent magnets.

ACKNOWLEDGMENTS

The financial support from the German federal state of Hessen through its excellence programme LOEWE

RESPONSE and the German Science Foundation (DFG Xu121/7-1) is appreciated. The authors also greatly appreciate their access to the Lichtenberg High Performance Computer of Technische Universität Darmstadt.

- [1] H. Zheng, J. Wang, S.E. Lofland, Z. Ma, L. Mohaddes-Ardabili, T. Zhao, L. Salamanca-Riba, S.R. Shinde, S.B. Ogale, F. Bai, D. Viehland, Y. Jia, D.G. Schlom, M. Wuttig, A. Roytburd, and R. Ramesh, Multiferroic BaTiO₃-CoFe₂O₄ nanostructures, *Science* **303**, 661 (2004).
- [2] Y. Wang, J. Hu, Y. Lin, and C.-W. Nan, Multiferroic magnetoelectric composite nanostructures, *NPG Asia Mater.* **2**, 61 (2010).
- [3] M. Yi, B.-X. Xu, and Z. Shen, Effects of magnetocrystalline anisotropy and magnetization saturation on the mechanically induced switching in nanomagnets, *J. Appl. Phys.* **117**, 103905 (2015).
- [4] N. Tiercelin, Y. Dusch, S. Giordano, A. Klimov, V. Preobrazhensky, and P. Pernod, in *Nanomagnetic and Spintronic Devices for Energy-Efficient Memory and Computing*, edited by J. Atulasimha and S. Bandyopadhyay (Wiley, New York, 2016), p. 221.
- [5] M. Yi, B.-X. Xu, and D. Gross, Mechanically induced deterministic 180° switching in nanomagnets, *Mech. Mater.* **87**, 40 (2015).
- [6] J.-M. Hu, L.-Q. Chen, and C.-W. Nan, Multiferroic heterostructures integrating ferroelectric and magnetic materials, *Adv. Mater.* **28**, 15 (2016).
- [7] M. Yi, B.-X. Xu, and Z. Shen, 180° magnetization switching in nanocylinders by a mechanical strain, *Extreme Mech. Lett.* **3**, 66 (2015).
- [8] T.G. Woodcock, Y. Zhang, G. Hrkac, G. Ciuta, N.M. Dempsey, T. Schrefl, O. Gutfleisch, and D. Givord, Understanding the microstructure and coercivity of high performance NdFeB-based magnets, *Scr. Mater.* **67**, 536 (2012).
- [9] G. Hrkac, T.G. Woodcock, K. T. Butler, L. Saharan, M. T. Bryan, T. Schrefl, and O. Gutfleisch, Impact of different Nd-rich crystal-phases on the coercivity of Nd-Fe-B grain ensembles, *Scr. Mater.* **70**, 35 (2014).
- [10] A. Kubo, J. Wang, and Y. Umeno, Development of interatomic potential for Nd-Fe-B permanent magnet and evaluation of magnetic anisotropy near the interface and grain boundary, *Model. Simul. Mater. Sci. Eng.* **22**, 065014 (2014).
- [11] G. Hrkac, K. Butler, T.G. Woodcock, L. Saharan, T. Schrefl, and O. Gutfleisch, Modeling of Nd-oxide grain boundary phases in Nd-Fe-B sintered magnets, *JOM* **66**, 1138 (2014).
- [12] G. Hrkac, T.G. Woodcock, C. Freeman, A. Goncharov, J. Dean, T. Schrefl, and O. Gutfleisch, The role of local anisotropy profiles at grain boundaries on the coercivity of Nd₂Fe₁₄B magnets, *Appl. Phys. Lett.* **97**, 232511 (2010).
- [13] S. Bance, H. Oezelt, T. Schrefl, G. Ciuta, N.M. Dempsey, D. Givord, M. Winklhofer, G. Hrkac, G. Zimanyi, O. Gutfleisch, T.G. Woodcock, T. Shoji, M. Yano, A. Kato, and A. Manabe, Influence of defect thickness on the angular dependence of coercivity in rare-earth permanent magnets, *Appl. Phys. Lett.* **104**, 182408 (2014).

- [14] T. G. Woodcock, Q. M. Ramasse, G. Hrkac, T. Shoji, M. Yano, A. Kato, and O. Gutfleisch, Atomic-scale features of phase boundaries in hot deformed Nd-Fe-Co-B-Ga magnets infiltrated with a Nd-Cu eutectic liquid, *Acta Mater.* **77**, 111 (2014).
- [15] B. E. Davies, R. S. Mottram, and I. R. Harris, Recent developments in the sintering of NdFeB, *Mater. Chem. Phys.* **67**, 272 (2001).
- [16] O. Gutfleisch, M. A. Willard, E. Brück, C. H. Chen, S. G. Sankar, and J. P. Liu, Magnetic materials and devices for the 21st century: Stronger, lighter, and more energy efficient, *Adv. Mater.* **23**, 821 (2011).
- [17] S. Sawatzki, C. Kübel, S. Ener, and O. Gutfleisch, Grain boundary diffusion in nanocrystalline Nd-Fe-B permanent magnets with low-melting eutectics, *Acta Mater.* **115**, 354 (2016).
- [18] K. Löewe, C. Brombacher, M. Katter, and O. Gutfleisch, Temperature-dependent Dy diffusion processes in Nd-Fe-B permanent magnets, *Acta Mater.* **83**, 248 (2015).
- [19] C. H. de Groot and K. de Kort, Magnetoelastic anisotropy in NdFeB permanent magnets, *J. Appl. Phys.* **85**, 8312 (1999).
- [20] Y. Murakami, T. T. Sasaki, T. Ohkubo, and K. Hono, Strain measurements from Nd₂Fe₁₄B grains in sintered magnets using artificial moiré fringes, *Acta Mater.* **101**, 101 (2015).
- [21] Y. Murakami, K. Niitsu, S. Kaneko, T. Tanigaki, T. Sasaki, Z. Akase, D. Shindo, T. Ohkubo, and K. Hono, Strain measurement in ferromagnetic crystals using dark-field electron holography, *Appl. Phys. Lett.* **109**, 193102 (2016).
- [22] H. Moriya, H. Tsuchiura, and A. Sakuma, First principles calculation of crystal field parameter near surfaces of Nd₂Fe₁₄B, *J. Appl. Phys.* **105**, 07A740 (2009).
- [23] T. Suzuki, Y. Toga, and A. Sakuma, Effects of deformation on the crystal field parameter of the Nd ions in Nd₂Fe₁₄B, *J. Appl. Phys.* **115**, 17A703 (2014).
- [24] S. Tanaka, H. Moriya, H. Tsuchiura, A. Sakuma, M. Diviš, and P. Novák, First principles study on the local magnetic anisotropy near surfaces of Dy₂Fe₁₄B and Nd₂Fe₁₄B magnets, *J. Appl. Phys.* **109**, 07A702 (2011).
- [25] Y. Toga, T. Suzuki, and A. Sakuma, Effects of trace elements on the crystal field parameters of Nd ions at the surface of Nd₂Fe₁₄B grains, *J. Appl. Phys.* **117**, 223905 (2015).
- [26] S. Tanaka, H. Moriya, H. Tsuchiura, A. Sakuma, M. Diviš, and P. Novák, First-principles calculation of crystal field parameters of Dy ions substituted for Nd in Nd-Fe-B magnets, *J. Phys. Conf. Ser.* **266**, 012045 (2011).
- [27] Y. Tatetsu, S. Tsuneyuki, and Y. Gohda, First-Principles Study of the Role of Cu in Improving the Coercivity of Nd-Fe-B Permanent Magnets, *Phys. Rev. Applied* **6**, 064029 (2016).
- [28] N. Drebov, A. Martinez-Limia, L. Kunz, A. Gola, T. Shigematsu, T. Eckl, P. Gumbsch, and C. Elsässer, *Ab initio* screening methodology applied to the search for new permanent magnetic materials, *New J. Phys.* **15**, 125023 (2013).
- [29] I. Kitagawa and Y. Asari, Magnetic anisotropy of R₂Fe₁₄B (R = Nd, Gd, Y): Density functional calculation by using the linear combination of pseudo-atomic-orbital method, *Phys. Rev. B* **81**, 214408 (2010).
- [30] A. Asali, P. Toson, P. Blaha, and J. Fidler, Dependence of magnetic anisotropy energy on *c/a* ratio of X₂Fe₁₄B (X = Y, Pr, Dy), *IEEE Trans. Magn.* **50**, 1 (2014).
- [31] Z. Torbatian, T. Ozaki, S. Tsuneyuki, and Y. Gohda, Strain effects on the magnetic anisotropy of Y₂Fe₁₄B examined by first-principles calculations, *Appl. Phys. Lett.* **104**, 242403 (2014).
- [32] G. Kresse and J. Furthmüller, Efficient iterative schemes for *ab initio* total-energy calculations using a plane-wave basis set, *Phys. Rev. B* **54**, 11169 (1996).
- [33] J. P. Perdew, K. Burke, and M. Ernzerhof, Generalized Gradient Approximation Made Simple, *Phys. Rev. Lett.* **77**, 3865 (1996).
- [34] M. J. Donahue and D. G. Porter, OOMMF software package, <http://math.nist.gov/oommf> (2016).
- [35] T. L. Gilbert, A phenomenological theory of damping in ferromagnetic materials, *IEEE Trans. Magn.* **40**, 3443 (2004).
- [36] M. Yi and B.-X. Xu, A constraint-free phase field model for ferromagnetic domain evolution, *Proc. R. Soc. A* **470**, 20140517 (2014).
- [37] M. Yi and B.-X. Xu, A real-space and constraint-free phase field model for the microstructure of ferromagnetic shape memory alloys, *Int. J. Fract.* **202**, 179 (2016).
- [38] H. Sepehri-Amin, T. Ohkubo, M. Gruber, T. Schrefl, and K. Hono, Micromagnetic simulations on the grain size dependence of coercivity in anisotropic Nd-Fe-B sintered magnets, *Scr. Mater.* **89**, 29 (2014).
- [39] A. A. Griffith, The phenomena of rupture and flow in solids, *Phil. Trans. R. Soc. A* **221**, 163 (1921).
- [40] N. C. Koon, B. N. Das, M. Rubinstein, and J. Tyson, Magnetic properties of R₂Fe₁₄B single crystals, *J. Appl. Phys.* **57**, 4091 (1985).
- [41] M. Sagawa, S. Fujimura, H. Yamamoto, Y. Matsuura, and S. Hirosawa, Magnetic properties of rare-earth-iron-boron permanent magnet materials, *J. Appl. Phys.* **57**, 4094 (1985).
- [42] O. Yamada, H. Tokuhara, F. Ono, M. Sagawa, and Y. Matsuura, Magnetocrystalline anisotropy in Nd₂Fe₁₄B intermetallic compound, *J. Magn. Magn. Mater.* **54-57**, 585 (1986).
- [43] Y. Otani, H. Miyajima, and S. Chikazumi, Magnetocrystalline anisotropy in Nd-Fe-B magnet, *J. Appl. Phys.* **61**, 3436 (1987).
- [44] D. Givord, H. S. Li, J. M. Moreau, R. P. de la Bâthie, and E. D. T. de Lacheisserie, Structural and magnetic properties in R₂Fe₁₄B compounds, *Physica (Amsterdam)* **130B+C**, 323 (1985).
- [45] J. F. Herbst, Nd₂Fe₁₄B materials: Intrinsic properties and technological aspects, *Rev. Mod. Phys.* **63**, 819 (1991).
- [46] L. Nordstrom, B. Johansson, and M. S. S. Brooks, Calculation of the electronic structure and the magnetic moments of Nd₂Fe₁₄B, *J. Phys. Condens. Matter* **5**, 7859 (1993).
- [47] S. S. Jaswal, Electronic structure and magnetism of R₂Fe₁₄B (R = Y, Nd) compounds, *Phys. Rev. B* **41**, 9697 (1990).
- [48] I. Kitagawa, Calculation of electronic structures and magnetic moments of Nd₂Fe₁₄B and Dy₂Fe₁₄B by using linear-combination-of-pseudo-atomic-orbital method, *J. Appl. Phys.* **105**, 07E502 (2009).

- [49] Z.-Q. Gu and W. Y. Ching, Comparative studies of electronic and magnetic structures in $Y_2Fe_{14}B$, $Nd_2Fe_{14}B$, $Y_2Co_{14}B$, and $Nd_2Co_{14}B$, *Phys. Rev. B* **36**, 8530 (1987).
- [50] W. Y. Ching and Z.-Q. Gu, Electronic structure of $Nd_2Fe_{14}B$, *J. Appl. Phys.* **61**, 3718 (1987).
- [51] P. Morin and D. Schmitt, in *Handbook of Ferromagnetic Materials*, Vol. 5, edited by E. P. Wohlfarth and K. H. J. Buschow (North-Holland, Amsterdam, 1990), p. 1.
- [52] G. A. Zickler, P. Toson, A. Asali, and J. Fidler, Nano-analytical TEM studies and micromagnetic modelling of Nd-Fe-B magnets, *Phys. Procedia* **75**, 1442 (2015).
- [53] M. Yi, O. Gutfleisch, and B.-X. Xu, Micromagnetic simulations on the grain shape effect in Nd-Fe-B magnets, *J. Appl. Phys.* **120**, 033903 (2016).
- [54] S. Erokhin and D. Berkov, Optimization of Nanocomposite Materials for Permanent Magnets: Micromagnetic Simulations of the Effects of Intergrain Exchange and the Shapes of Hard Grains, *Phys. Rev. Applied* **7**, 014011 (2017).
- [55] S. Bance, J. Fischbacher, T. Schrefl, I. Zins, G. Rieger, and C. Cassignol, Micromagnetics of shape anisotropy based permanent magnets, *J. Magn. Magn. Mater.* **363**, 121 (2014).
- [56] S. Bance, B. Seebacher, T. Schrefl, L. Exl, M. Winklhofer, G. Hrkac, G. Zimanyi, T. Shoji, M. Yano, N. Sakuma, M. Ito, A. Kato, and A. Manabe, Grain-size dependent demagnetizing factors in permanent magnets, *J. Appl. Phys.* **116**, 233903 (2014).
- [57] T. Schrefl, J. Fidler, and H. Kronmüller, Nucleation fields of hard magnetic particles in 2D and 3D micromagnetic calculations, *J. Magn. Magn. Mater.* **138**, 15 (1994).